POAC'13
Espoo, Finland

Proceedings of the 22nd International Conference on
Port and Ocean Engineering under Arctic Conditions
June 9-13, 2013
Espoo, Finland

Analysis of Tidal Deformations of Land Fast Ice in Shallow Arctic Fjord

David Wrangborg [1,2], Rylan Grady [3], Aleksey Marchenko [1,2], Evgeny Karulin[4]

[1] Sustainable Arctic Marine and Coastal Technology (SAMCoT), Centre for Research-based Innovation (CRI), Norwegian University of Science and Technology, Trondheim, Norway

[2] The University Centre in Svalbard, Longyearbyen, Norway

[3] Pomona College, California, USA

[4]Krylov Ship Building Research Institute, St.-Petersburg, Russia

ABSTRACT

The paper is devoted to the investigation of ice deformations and ice stresses build up in shore line zone of Sveasundet in Svea Bay of the Van Mijen Fjord in Spitsbergen. Two field surveys were performed in 2011 and 2012 for the monitoring of ice deformations induced by semidiurnal tides. A Leica Total Station and Laser Scanner Riegl VZ-1000 were used in the field measurements. Significant deflections of the ice surface from the horizontal plane were detected at low tide phases. Measurements of ice stresses near the shoreline indicated their semidiurnal oscillations with maximal onshore stresses at high tide. Mathematical model and numerical simulations were performed to explain the buildup and concentration of the ice stresses near narrow tips of the shoreline.

1. INTRODUCTION

The natural environment of large areas on the arctic shelf is characterized by small water depth, long ice season, strong winds, low air temperatures, tides with current velocities up to 1 m/s and water level variations of about 1 m. Formation of seasonal frozen soils and degradation of the permafrost are typical processes in coastal zones. Estimates of design loads on arctic coastal structures should be performed using actual field data. Overestimates of design loads lead to a significant increase of the costs for the construction of engineering structures, while underestimates can cause catastrophic results.

The region of the case study is located in the Van Mijen Fjord near mining settlement Svea in Spitsbergen (Fig. 1). It is characterised by shallow water depth, a tidal variability from 0.5 m at neap to 2 m at spring tides, an ice cover with thicknesses up to 1 m and a modest river runoff from Braganzavågen. Usually the sea surface in the fjord is covered by ice from the end of January to the end of June. The mean depth across the fjord varies within 1 - 5 meters over the cycle of semidiurnal tide with period 12.42 h. The ice can be grounded at low tide in very shallow water in the central part of the fjord visible as dark regions in Fig. 2a. Ice drilling has shown that the seabed soil was frozen when the ice was grounded, and it was not frozen when a water layer with a thickness of a few centimetres was observed below the ice.

The ice surface shape is not flat in low tide because of the grounding. In high tide the ice surface is more flat (Marchenko et al., 2008).

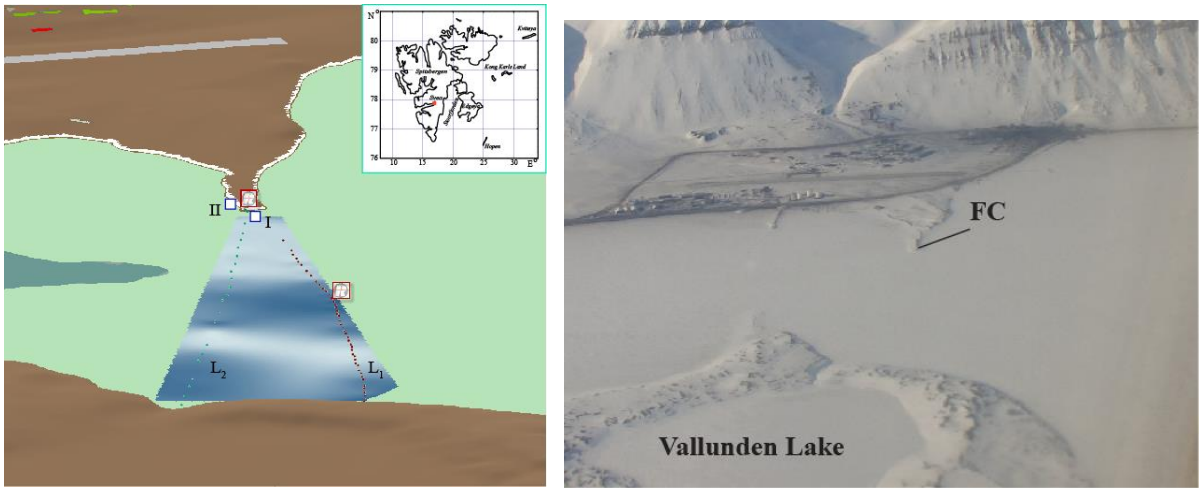

a) b)

Figure 1. Region of field works: ArcView image (a) and aerial photograph in winter (b).

The shape of ice surface cross the fjord was reconstructed by the measurements of the distance from seabed to ice surface in several holes drilled through the ice. Each measurement was been done within 0.5 hour by crossing of the fjord by snow scooter. It was discovered that absolute value of the slope angle of ice surface reaches 0.02 in low tide. Depending on snow thickness and tidal phase sea water flooding the ice was observed in different locations across the fjord.

a) b)

Figure 2. Aerial photograph of the study region in summer (a). Locations of ice pressure measurements near the cabin (b).

The formation of ice stresses near the tip of a breakwater in Svea Bay was studied by Caline and Barrault (2008). Six stress sensors were frozen-in in two rosettes nearby a breakwater at 15 cm depth on each side of a tidal crack from 6 to 11 May 2007 near the breakwater (Location I in Fig. 1b and 2b). The tidal movement of the ice was recorded with differential GPS equipment a week later. The tide is being recorded continuously in the area and the stresses in the active zone were investigated depending on the tide. Maximal compressions up to 200 kPa were systematically detected in low tide in the along shoreline direction. Sensor measuring ice pressure in perpendicular direction to the shoreline recorded maximal pressure up to 100 kPa at high tide.

In the present paper we investigate the origin of ice stresses near the shoreline. It is assumed that observed flattening of the ice surface at high tide can influence a confinement and stresses near the shoreline. Input data for the modelling should include information about 3D shape of the ice surface and realistic configuration of the computational domain repeating shoreline configuration. Mathematical model describing the build-up of in plane ice stresses is based on Foppl - von Karman equations describing large deflection of thin flat plates (Foppl, 1907). In this approach the in-plane strains are proportional to the second order products of deflection gradient components. A set of 3d point clouds recorded using a Riegl VZ-1000 laser scanner during a cycle from low to high tide provided input data on 3D shape of the ice surface. The paper is organized as follows. In the second section the results of laser scanner survey are described. Results of ice stress measurements are presented in the third section. Mathematical model and results of numerical simulations are described in the fourth section. Main results of the investigations are summarised in the conclusions.

2. TOTAL STATION SURVEY

The Total Station Leica (TS) survey was performed in the March 22-24, 2011. The air temperatures in the winter 2011 were low, and ice thickness in the range of the filed works exceeded 1 m. The TS was installed on top of the cabin (Fig. 2b). Some test points were taken to test the range of the TS. In good conditions it was possible to measure a distance over 1700 m. A grid was made with a distance of approximately 200 m times 200 m between the measuring points. The total grid was approximately 2 km times 1 km (Fig. 3a). The TS registered vertical displacements of reflectors fixed on the ice in the grid points. The grid was set up by using a GPS marking the grid points. The scooters drove 200 m and put down a stick into each grid point. To get a straight line two scooters drove 200 m on each side, turned against each other and drove after the light of the other scooter. If there were no sticks available a pile of snow was dug to mark the point. The grid was organized into 12 rows. The rows are oriented southeast – northwest. Row 1 is located at the most western point of the grid. When measuring, one person operated the TS from the cabin roof, and two persons drove a route around the grid. One person navigating and one person operated the reflector-prism (Fig. 3b). Communication between the scooter and the TS operator was done by using a VHF radio.

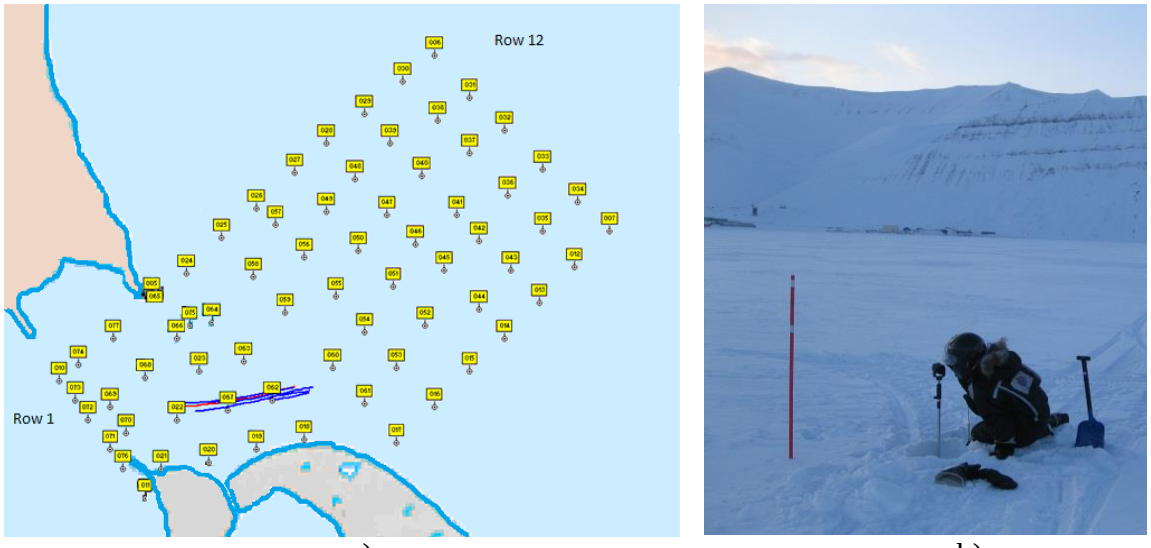

a) b)

Figure 3. Positions of reflectors for the monitoring of the ice deflection with Total station (a). Fragment of field works with reflector (b).

Measurements were performed around events of low tide and high tide. One round of measurements over the entire grid took about 1 hour. Examples of measurements results are presented in Fig. 4 and Fig.5. From the profile shown in Fig. 4 follows that the shape of the ice surface is almost flat in high tide, and deflected in low tide. The shape of the ice surface is varying significantly over the tide. The slope angle of the ice surface reached 0.2^{o} or 1.5 m deflection over 400 m length (Fig. 4). Assuming that distance between neighbour points in Fig. 4 is equal 200 m we find that distance between points 1 and 5 in Fig. 4 is about 1 km. The increase of the ice surface length between points 1 and 5 is about 2 cm when the ice surface is deformed from the horizontal position to the low tide position measured on 24.03 at 11:00. Therefore the ice lengthening is equal to 0.00002. Estimating compressive stress with the formula $\sigma = E\varepsilon$ we find that $\sigma = 20\,\text{kPa}$ when $E = 1\,\text{GPa}$ and $\varepsilon = 0.00002$. This value estimates the lower bound of compressive stresses on the shoreline. It is smaller than the stresses 70 kPa measured in perpendicular to shoreline direction and near the shore by Caline and Barrault (2008).

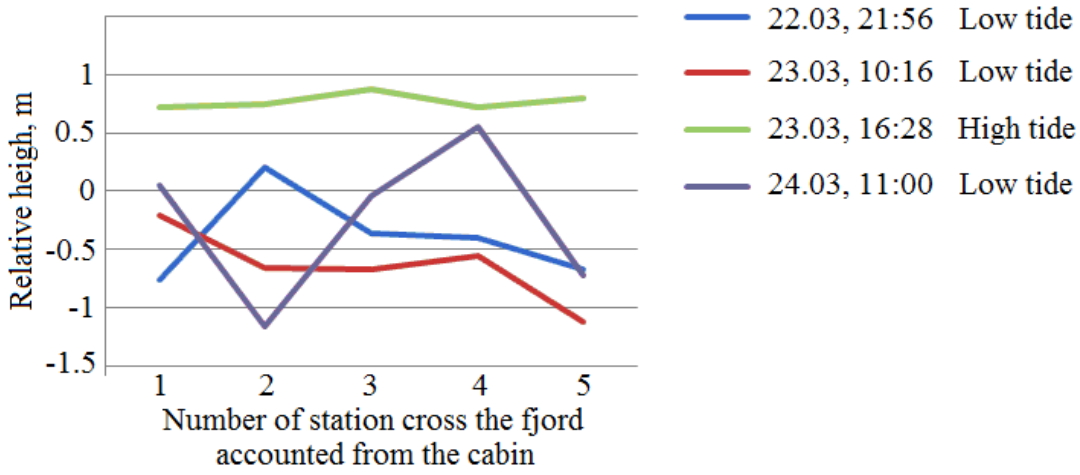

Figure 4. Examples of measured ice profiles cross the fjord in low and high tides.

3D shapes of the ice cover surface are shown in Fig. 5 in low tide and high tide events. Red colors show elevations and blue colors show depressions of the ice surface. It is visible that in the central part of the fjord the ice is sitting at the bottom ridge (see e.g., upper left Fig. 5). The bottom ridges are visible on summer aerial photographs (Fig. 2a). The shape of the ice surface has well recognized 3D features showing complicated ways for the water penetration below the ice. The tidal amplitude was of the same order as in ice free season. Blue lines in Fig. 3a show cracks formed in the ice when it is interacting with the bottom ridge.

3. LASER SCANNER SURVEY

The Laser Scanner Riegl VZ-1000 (LS) survey was performed in the March 22-25, 2012. According to the description the scanning could be possible over up to 1.4 km range with spatial resolution below 1 cm. The LS was setup on the roof of a cabin at the tip of Barrynestet overlooking the inlet between Sveasundet and Braganzavågen on the March 22-23 (Fig. 2b). Originally we hope to capture the entirety of Sveasundet across to Vallunden Lake (Fig. 1b). However the range of the scanner proved far too limited on flat snow surface to be able to accomplish this. The range achieved were about 200 m which meant only about a third of the width of the inlet was covered by scanning from the cabin. A scan was made every half hour starting from around low tide (09:49) to around high tide (14:48). The times of the scanning are presented in Fig. 6a according to the tidal phase. The water level elevation was measured with the sensor SBE 37 deployed at the sea bottom near the cabin with sampling interval 2 min. The evolution of the ice foot shape reconstructed with the Laser

scanner images is presented in Fig. 7. The break points at 8 and 13 m on the graphs correspond to the tidal cracks extending through the ice in parallel direction to the shoreline. In our opinion these crack are very important for the stress build up in the hinge zone near the shoreline.

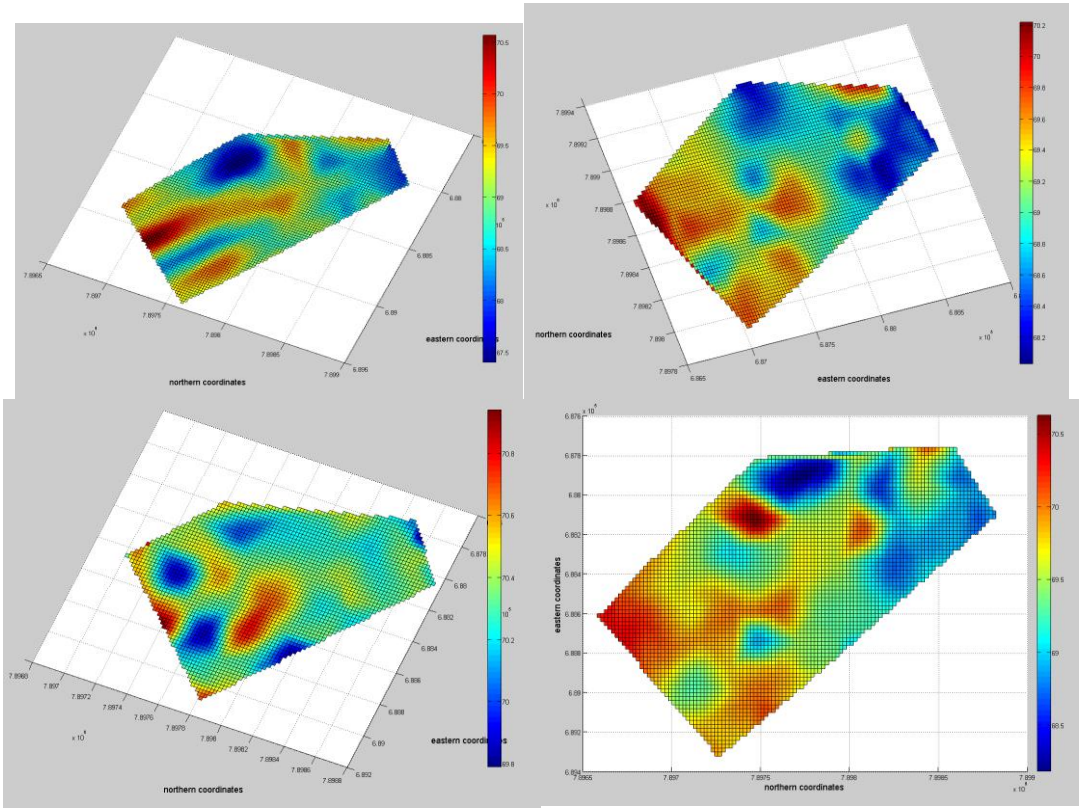

Figure 5. Colored plots of the ice surface in 2011. From the top left: Low tide 22.03, 21:56; Low tide 23.03, 10:16; High tide 22.03, 16:28; Low tide 24.03, 11:00.

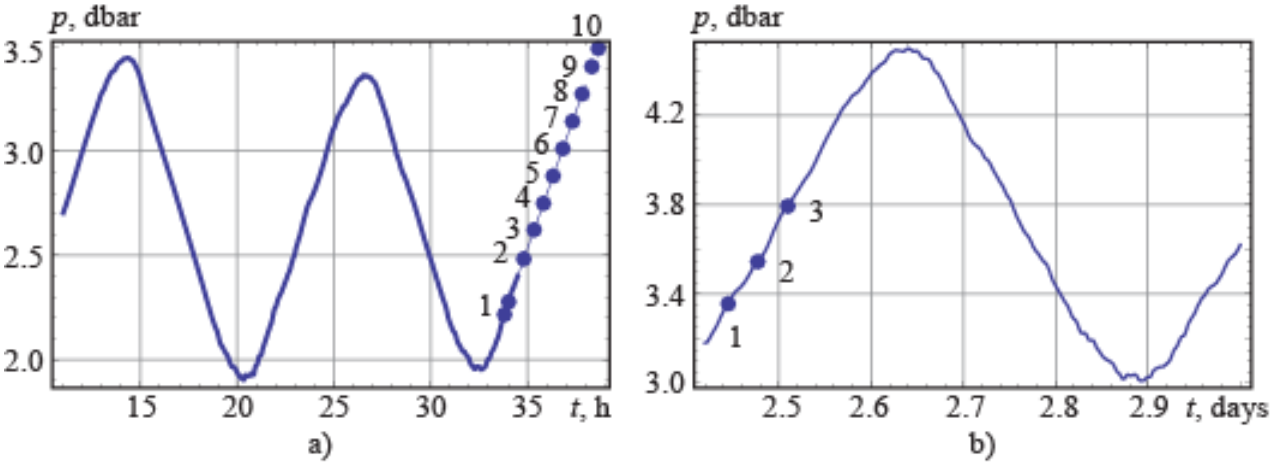

Figure 6. Time of the laser scanning is shown according to the tidal phase on March 22-23 (a) and March 24-25 (b). Time is counted from 00:00 on March 22. (1 dbar = 0.01 mbar)

Relative shortening of the distance between the points of the ice surface located on distances 7 m and 20 m is about $\varepsilon \approx 5.8 \cdot 10^{-3}$. This deformation creates compressive stress $\sigma = 5.8\,\mathrm{MPa}$ when the effective elastic modulus is $E = 1\,\mathrm{GPa}$. Deformations observed on the ice surface (Fig. 7) show that ice creep and crack opening are important for the reduction of stresses near the shoreline.

In addition, in a try to remedy the range limit, three scans where made from the ice above the underwater ridge on the following day the March 24 (Fig. 1a). During post processing the positioning of the scanner on that location proved problematic. The scanning time was about half an hour and during that time not only did the scanner change its vertical position with the ice but also tilted a small but vital amount as the shape of the bulge of the ice, caused by the beaching on the ridge, changed a little bit. This has a warping effect on the scans. The amount of the warp is impossible to determine in retrospect. Combination of three scanner images from the ridge with suitable scans from the cabin made it possible to cover almost all the surface of ice over the inlet (Fig. 8a). However the accuracy of the final results might not be as good as single scan would give because the combination of two days and the problems encountered when scanning from the ice. Two examples of ice surface profiles scanned in almost low tide (point 1 in Fig. 6b) and in intermediate tide (point 3 in Fig. 6b) are shown in Fig. 8b.

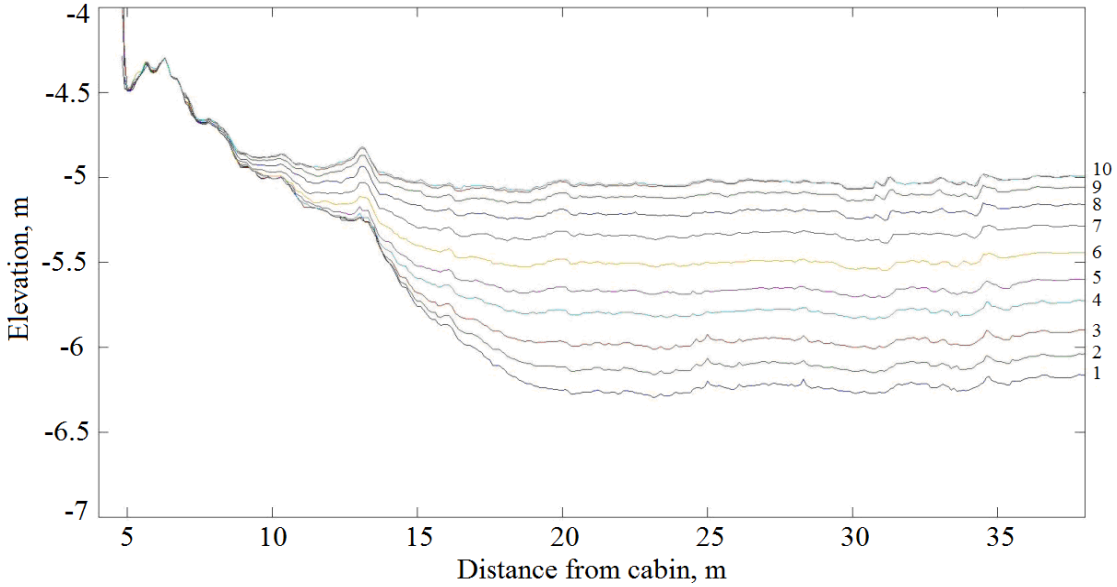

Figure 7. Cross-sectional results made from scanning data on March 23 showing the movement of the ice during the tidal cycle. Scanner is installed on top of the cabin.

Although entire profiles of the ice surface were constructed using different scans some features of the ice cross-section in Fig. 8b is a product of single scans. For example, each of segments on curves 1 and 3 bounded by two vertical dashed lines in Fig. 8b made entirely of the scan data from the ice. The length of the blue curve segment bounded by the dashed lines is 65.0013 m and the length of the red curve segment bounded by the dashed lines is 65.0002 m. Thus the compressive strain of the ice in the cross-sectional direction is $\varepsilon \approx 1.7 \cdot 10^{-5}$. Therefore compressive stresses on this ice segment are about $\sigma = 17\,\mathrm{kPa}$ when the effective elastic modulus is $E = 1\,\mathrm{GPa}$.

Grounded ice was registered also with antenna EM-31 (Geonics) working in the ice thickness measurement mode. Ice thickness measurements were performed along lines L_1 and L_2 shown in Fig. 1a. The antenna showed very high ice thickness in places where the ice was grounded. These locations are shown in Fig. 1a by dark blue colours. In light regions the ice thickness was 0.5 m.

4. MEASUREMENTS OF ICE STRESSES

Measurements of ice stress in perpendicular direction to the shoreline were performed with the same equipment (oil pressure membrane) as in the works of Caline and Barrault (2008) but in different location II shown in Fig. 1a, Fig. 2b and Fig. 9a. Sampling interval of the measurements was equal to 1 s. Two measurement series were performed over full tidal cycle as it is shown in Fig. 9b by grey color. After the freeze-in the sensors in the ice they showed constant high pressure about 330 kPa. This constant pressure is not removed from the records shown in Fig. 10. Time locations of registered local maxima of the stresses are marked in Fig. 9b by dashed lines. It is visible that all local maxima are very close to high tide or low tide events. The amplitude of the stress variations is changing from 5 kPa to 15 kPa.

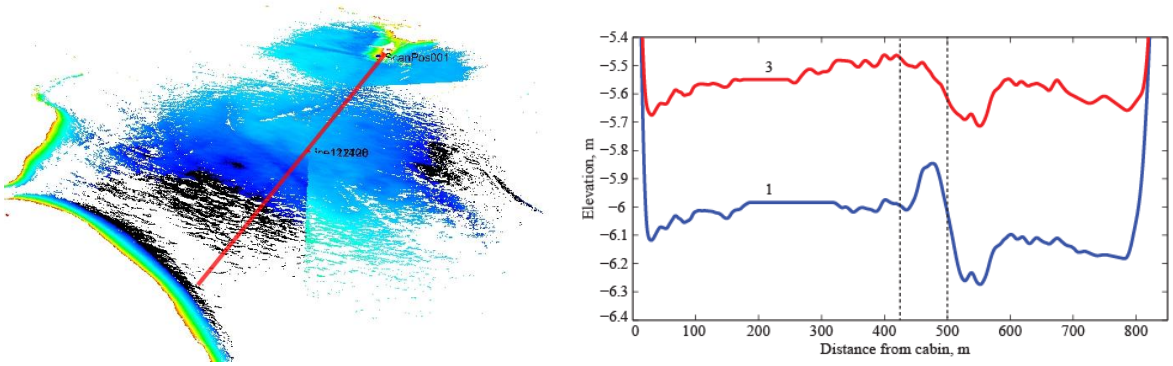

a) b)

Figure 8. Scans made from the cabin and ice on March 24-25 registered and showed colored by height (a). Direction of cross-section shown in red. The shape of sea ice along the cross-section in the times 1 and 3 (Fig. 3b).

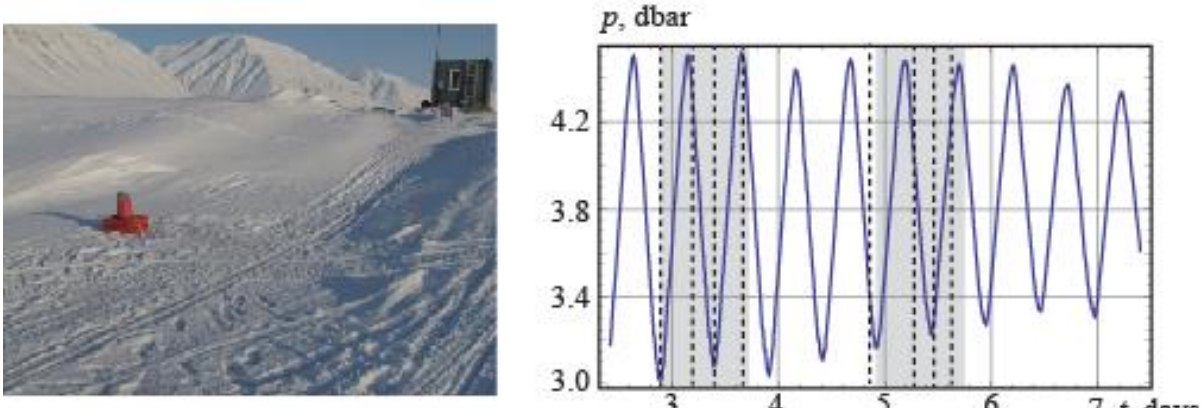

a) b)

Figure 9. Location of ice stress measurements (a), records of water pressure at the bottom (b). (1 dbar = 0.01 mbar)

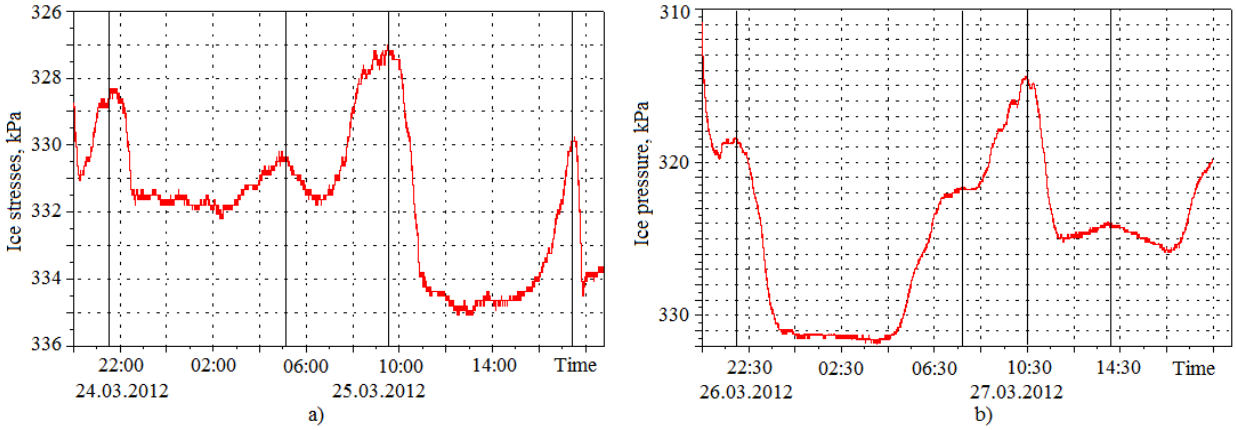

Figure 10. Records of the stress sensor on March 24-25 (a) and March 26-27 (b).

5. NUMERICAL SIMULATIONS

Mathematic model used in numerical simulations is based on the same approach as in the Foppl - von Karman equations describing large deflection of thin flat plates (Landau and Lifshitz, 1970). However we don't use the Foppl - von Karman equations directly because their solution is not available in Comsol Multiphysics 4.3a. Numerical simulations in Comsol Multiphysics 4.3a are performed in linear elastic module with specific external force. The equations used for the modelling are derived below. In our simulations we consider only ice stresses build up due to the ice grounding on the bottom ridge of cylindrical shape. The deflections of ice near shoreline are excluded from the consideration.

Length of a deformed element belonging to the neutral surface of the ice is expressed by the formula (Landau and Lifshitz, 1970)

$$dl^2 = (dx_1 + du_1)^2 + (dx_2 + du_2)^2 + d\eta^2, \qquad (1)$$

where $\mathbf{u} = (u_1, u_2)$ is the displacement vector, and $z = \eta(x_1, x_2)$ is the deflection of the ice in the vertical direction. Assuming that $du_\alpha = (\partial u_\alpha / \partial x_1)dx_1 + (\partial u_\alpha / \partial x_2)dx_2$, and $d\eta = (\partial \eta / \partial x_1)dx_1 + (\partial \eta / \partial x_2)dx_2$ we find

$$dl^2 = dl_0^2 + \sum_{\alpha,\beta} 2\varepsilon_{\alpha\beta} dx_\alpha dx_\beta, \quad \varepsilon_{\alpha\beta} = \varepsilon^p_{\alpha\beta} + \varepsilon^b_{\alpha\beta}, \qquad (2)$$

$$\varepsilon^p_{\alpha\beta} = \frac{1}{2}\left(\frac{\partial u_\alpha}{\partial x_\beta} + \frac{\partial u_\beta}{\partial x_\alpha}\right) \varepsilon^b_{\alpha\beta} = \frac{1}{2}\frac{\partial \eta}{\partial x_\alpha}\frac{\partial \eta}{\partial x_\beta},$$

where $(\alpha, \beta) = (1,2)$, the strains $\varepsilon^b_{\alpha\beta}$ are formed because of the deflection and the strains $\varepsilon^p_{\alpha\beta}$ are excited because of the boundary conditions.

Formulas (2) show that maximal tensile stresses are excited when the ice is deflected. In case under the consideration the opposite situation is assumed. Namely when the ice is deformed and grounded at the phase of low tide the deformations are assumed to be zero because of the ice cracking, and at the phase of high tide the ice is compressed. Thus the ice deformations are accounted from the deformed state at low tide and

$$\varepsilon_{\alpha\beta} = \varepsilon^p_{\alpha\beta} - \varepsilon^b_{\alpha\beta}. \qquad (3)$$

The strains $\varepsilon^p_{\alpha\beta}$ are formed due to the influence of the shoreline where the ice is fixed. The condition of strain compatibility is formulated for the plane problems in the form (Barber, 2002)

$$\frac{\partial^2 \varepsilon_{11}}{\partial x_2^2} + \frac{\partial^2 \varepsilon_{22}}{\partial x_1^2} = 2\frac{\partial^2 \varepsilon_{12}}{\partial x_1 \partial x_2}. \qquad (4)$$

Strains $\varepsilon_{\alpha\beta}^b$ don't satisfy this condition in general case. We consider in the present works a special case when $\eta = \eta(x_1, \varepsilon x_2)$ and small parameter $\varepsilon << 1$. In this case strains $\varepsilon_{\alpha\beta}^b$ satisfy condition (3) with accuracy $O(\varepsilon)$. The ice deflections near the shoreline are not described by this formula and their influence on the stresses is not considered within formulated approach.

In numerical simulations the deflection η is described by equation

$$\eta = A\cosh^{-2}(ax_1)\cosh^{-2}(\varepsilon a x_2), \qquad (5)$$

$$x_1 = k(x - x_r) + y - y_r,\ x_2 = k(y - y_r) - (x - x_r),\ k = y_r / x_r,$$

where the coordinates x and y are directed to the East and to the North, $x_r = 250\,\text{m}$, $y_r = -300\,\text{m}$, $A = 1.5\,\text{m}$, $a = 0.01\,\text{m}^{-1}$ and $\varepsilon = 0.1$. The counter lines and shape of the ice deflection are shown in Fig. 11, where all horizontal and vertical distances are shown in meters.

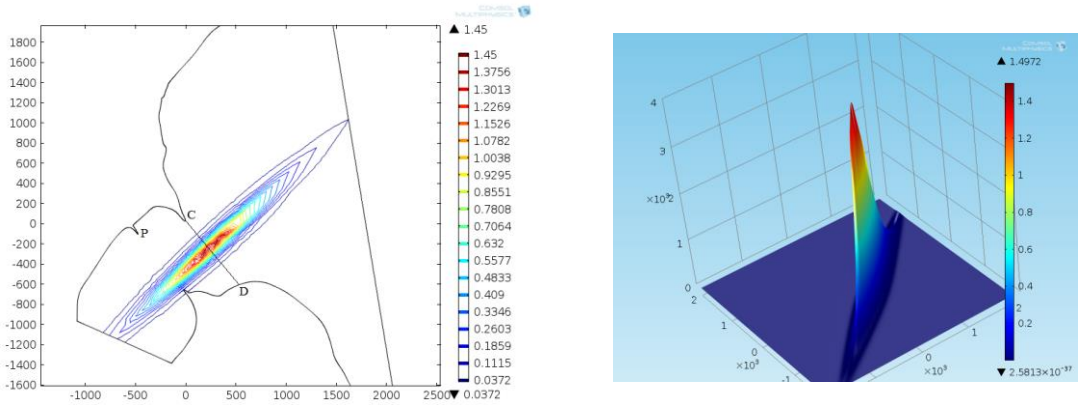

a) b)

Figure 11. The computational domain and contour lines of the ice surface deformed by the bottom ridge (a), and the ice surface shape (b).

The in-plane ice stresses $\sigma_{\alpha\beta}$ are related to the strains $\varepsilon_{\alpha\beta}$ according to the Hook's law

$$\sigma_{xx} = \frac{E}{1-\nu^2}\left(\varepsilon_{xx} + \nu\varepsilon_{yy}\right),\ \sigma_{yy} = \frac{E}{1-\nu^2}\left(\varepsilon_{yy} + \nu\varepsilon_{xx}\right),\ \sigma_{xy} = \frac{E}{1+\nu}\varepsilon_{xy}, \qquad (6)$$

where $E = 1\,\text{GPa}$ and $\nu = 0.33$ are Young's modulus and Poisson's ratio of the ice.

From formulas (3) follows

$$\sigma_{\alpha\beta} = \sigma_{\alpha\beta}^p - \sigma_{\alpha\beta}^b, \qquad (7)$$

where stresses $\sigma_{\alpha\beta}^p$ and $\sigma_{\alpha\beta}^b$ are expressed over the strains $\varepsilon_{\alpha\beta}^b$ and $\varepsilon_{\alpha\beta}^p$ by the formulas similar to (6).

The stresses $\sigma_{\alpha\beta}$ satisfy to the equations of static equilibrium. Substituting formulas (7) in the equations of static equilibrium we find that stresses $\sigma_{\alpha\beta}^p$ satisfies to static equilibrium equations with body force $\mathbf{F} = (F_x, F_y)$

$$\sum_{\alpha}\frac{\partial\sigma^{p}_{\alpha\beta}}{\partial x_{\alpha}}=F_{\beta}\,,\quad F_{\beta}=\sum_{\alpha}\frac{\partial\sigma^{b}_{\alpha\beta}}{\partial x_{\alpha}}\,. \tag{8}$$

Solution of equations (8) was constructed with Comsol Multiphysics 4.3a (Linear elastic material model) and boundary conditions assuming zero displacements u_{α} at the boundary of the computational domain shown in Fig. 11a. Figure 12 shows the ice pressure in the vicinity of the cabin C (Fig. 12a) calculated with the formula $p=-(\sigma_{xx}+\sigma_{yy})/2$. Concentrations of the pressure up to 60 kPa near the cabin C and up to 30 kPa near the pier P are visible in Fig. 12. The ice compression in other points near shoreline is much smaller.

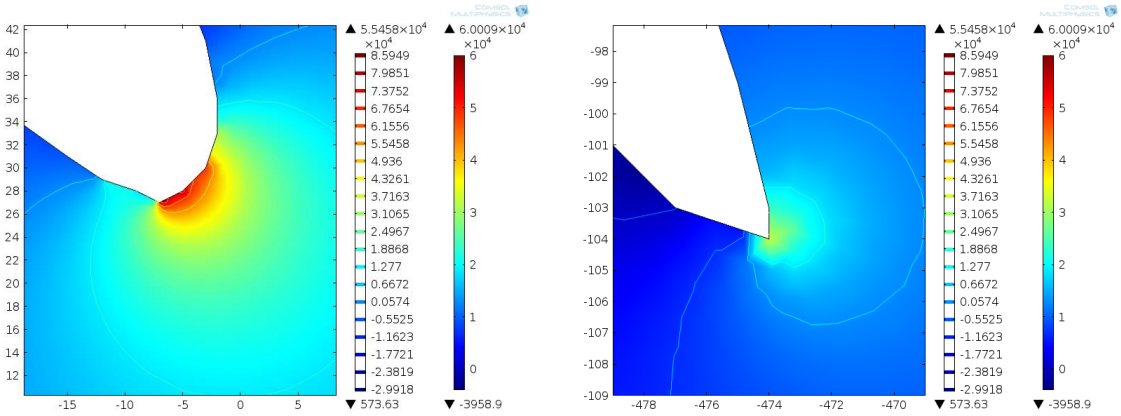

a) b)

Figure 12. Spatial distribution of ice stresses at high tide near the cabin C (a) and near the pier P (b).

5. CONCLUSIONS

Field surveys with the Total Station and laser scanner demonstrated three dimensional deformations of the sea ice surface at low tide in narrow part of Svea Bay. The amplitude of the ice surface deflection in low tide reaches 1 m over several hundred meter length cross the fjord. The deformations are caused by the grounding of the ice on the bottom ridges. The shape of the ice surface is not the same in each low tide. Ice thickness and tidal amplitude are most important for the ice shape at low tide. The ice is more flat at high tide. Observed deflections of sea ice over the semidiurnal tide are responsible for the formation of ice stresses near shoreline.

Deflections of sea ice in low tide are accompanied by the opening of cracks near shore line and around places where the ice is grounded. Radial and along shoreline cracks influence ice stresses near the shoreline. Displacements and bending deformations of grounded ice blocks can influence local compression at low tide and high tide near the shoreline. Cracks formed along the bottom ridge in the middle part of the fjord are opened in low tide and closed in high tide. This effect can influence the build-up of compressive stresses near the shore line at high tide. The build-up and concentration of compressive stresses near narrow shoreline tips is illustrated with numerical simulations using original simplified model constructed with the same assumption as the Foppl - von Karman equations describing large deflection of thin flat plates. Calculated compressive stresses about 60 kPa are closed to the values of stresses measured in front of the cabin in high tide.

In the modelling the ice is assumed to behave as linear elastic material. Sanderson (1988) demonstrated that representative time of creep buckling of floating ice is 45 hours when the stress is 0.25 MPa. This time is considerably larger than the time frame of tidal cycles. Effects

of creep, stress relaxation and crack opening are probably most important for the reduction of stresses induced by large deformations of ice near the shoreline.

ACKNOWLEDGEMENTS
The authors wish to acknowledge the support from the Research Council of Norway through the Centre for Research-based Innovation SAMCoT and the support from all SAMCoT partners.

REFERENCES
Barber, J. R., 2002. Elasticity - 2nd Ed., Kluwer Academic Publications.

Caline, F., and Barrault, S., 2008. Measurements of stresses in the coastal ice on both sides of a tidal crack. Proceedings of 19th IAHR International Symposium on Ice "Using New Technology to Understand Water-Ice Interaction", Vancouver, BC, Canada, July 6-11, 2008, Vol.2, 831-840.

Föppl, A., 1907. Vorlesungen über technische Mechanik, B.G. Teubner, Bd. 5., p. 132, Leipzig, Germany.

Landau, L.F., and Lifshitz, E.M., 1970. Theory of Elasticity, Volume 7 of A Course of Theoretical Physics, Pergamon Press.

Marchenko, A., Langen, I., and A. Shestov, 2009. Hydrological characteristics of a narrow and shallow part of Van Mijen fjord on Spitsbergen. Proceedings of Nineteenth (2009) International Offshore and Polar Engineering Conference (ISOPE), Osaka, Japan, June 21-26, TCP-689.

Sanderson T.J.O 1988, Ice Mechanics Risks to Offshore Structures. London Graham Trotham Limited. p. 150